One-micron resolution optical coherence tomography (OCT) in vivo for cellular level imaging

Gu, Jun; Shum, Ping; Liu, Linbo; Cui, Dongyao; Liu, Xinyu; Zhang, Jing; Yu, Xiaojun; Sun, Ding; Luo, Yuemei

2015

Cui, D., Liu, X., Zhang, J., Yu, X., Sun, D., Luo, Y., et al. (2015). One-micron resolution optical coherence tomography (OCT) in vivo for cellular level imaging. Proceeding of SPIE, 9312.

https://hdl.handle.net/10356/107371

https://doi.org/10.1117/12.2076438

One-micron resolution optical coherence tomography (OCT) in vivo for cellular level imaging

Dongyao Cui[1,3,4], Xinyu Liu[1], Jing Zhang[1], Xiaojun Yu[1], Sun Ding[1], Yuemei Luo[1], Jun Gu[1], Ping Shum[1,3,4], and Linbo Liu[1,2,3,*]

[1]School of Electrical and Electronic Engineering, Nanyang Technological University, Singapore 639798

[2]School of Chemical and Biomedical Engineering, Nanyang Technological University, Singapore 637459

[3]COFT, The Photonics Institute (TPI), Nanyang Technological University, Singapore 639798

[4]CINTRA CNRS/NTU/THALES, UMI 3288, Singapore 637553

ABSTRACT

We developed a spectral domain OCT system combining two NIR, CW light sources of different spectral range. Its resolving power is validated by visualizing the cellular structures of zebra fish larvae in vivo. An NIR extended illumination from 755-1100 nm is achieved. The axial resolution is 1.27 μm in air, corresponding to 0.93 μm in tissue (n=1.36), which is the highest axial resolution using NIR, CW laser sources up to date to the best of our knowledge. In vivo imaging is conducted to demonstrate the resolving power of proposed one-micron resolution OCT system. The top and bottom surfaces of individual disk-like red blood cell is reliably visualized, as well as flat, spindle shaped endothelial cells lining along the luminal surface of the blood vessel wall. This study provides a viable solution for cellular and subcellular level OCT imaging system which is also very competitive in cost.

Keywords: Optical Coherence Tomography (OCT), resolution, in vivo

1. INTRODUCTION

Optical coherence tomography (OCT) is a non-invasive, high-resolution, 3D (three dimensional) imaging technique that gains great developments in recent years for biomedical imaging [1]. Today, the system of optical coherence tomography has provided a possibility of analyzing tissue micro-structures at ~10-μm [2, 3]. Most recently researches of OCT are focused on higher resolution and increasing in imaging speed. To achieve cellular and sub-cellular level imaging, the axial resolution of OCT needs to reach ~1-μm to show the details of cellular and subcellular structures [4]. Past researches have reliably visualized biological microstructures using a class of ~1-μm OCT systems.

2. SYSTEM SETUP

NIR illumination of extended bandwidth from 755-1105nm was achieved in this ~1-μm OCT system using a combination of two light sources, Superlum Broadlighters T-850-HP(SLD arrays 1) of 3-dB spectral range from 755-930 nm and Exalos Ultra-Broadband EBS4C32 (SLD arrays 2) with 3-dB spectral range of 930-1105nm as depicted in figure 1. Two light sources were combined by a 70:30 non-polarizing cubic beam splitter (BS1) to balance the optical power at the output of the two light sources and directed to the desktop probe by a 50:50 non-polarizing cubic beam splitter (BS2) and a Nufern 780-HP single mode fiber (SMF). The beam was collimated by an achromat (L8, AC050-015-B, Thorlabs Inc.) of focal length 15mm and split into central circular reference wavefront and annular sample wavefront by a 45^{o} rod mirror (NT47-628, Edmund Optics Inc.). Incident beam was focused by objective lens (Mitutoyo Plan Apo NIR, 20X) of 10mm focal length and 70% transmission into a spot of size 1.7 μm. Light backreflected by reference mirror (RM) and backscattered by sample were recombined at the rod mirror and guided back to BS2 by SMF, where it is redirected to detection spectrometers after passing a 10μm pin hole. The signal was split into two beams by another 50:50 non-polarizating cubic beam splitter BS3 and detected by two synchronized spectrometers with Si camera (E2V, AViiVA EM4) and InGaAs camera (Sensors Unlimited GL2048L) respectively to achieve simultaneous dual spectrum detection of the entire spectrum. Two spectral interference patterns of ~50-nm spectral overlap were combined digitally afterward

Optical Coherence Tomography and Coherence Domain Optical Methods in Biomedicine XIX, edited by James G. Fujimoto, Joseph A. Izatt, Valery V. Tuchin, Proc. of SPIE Vol. 9312, 93123R · © 2015 SPIE · CCC code: 1605-7422/15/$18 · doi: 10.1117/12.2076438

to achieve the extended linewidth detection of ~293-nm. Both spectrometers consist of a camera lens (Nikon AF Nikkor 85mm f/1.8D) and a grating. 830 lines/mm reflective grating G1 (NT43-850, Edmund Optics Inc.) was used in spectrometer 1 whereas 1200 lines/mm transmission grating G2 (830 nm, Wasatch Photonics Inc.) was used in spectrometer 2. Spectral signal was digitized at 12-bit and transferred to a personal computer through camera link cables and an image acquisition board (KBN-PCE-CL4-F, Bitflow).

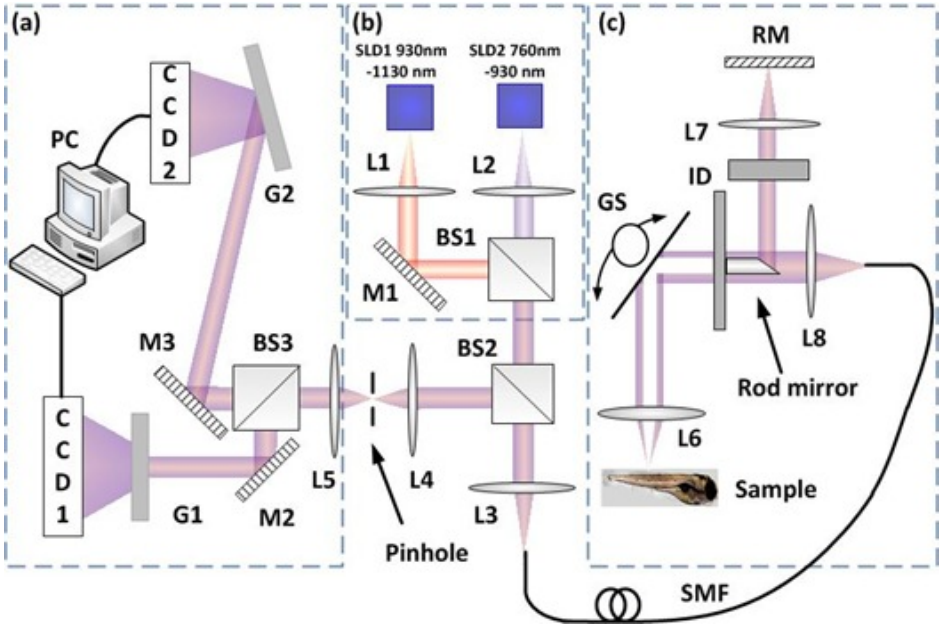

Figure 1: One-micrometer axial resolution optical coherence tomography system. L1-8: lenses. M1-3: mirrors. BS1-3: non-polarizing cube beam splitters. SMF: single mode fiber. RM: reference mirror. ID: iris diaphragm. G1-2: gratings. PC: personal computer. GS: galvo scanners.

3. SIGNAL ANALYSIS

3.1 Spectrum combination

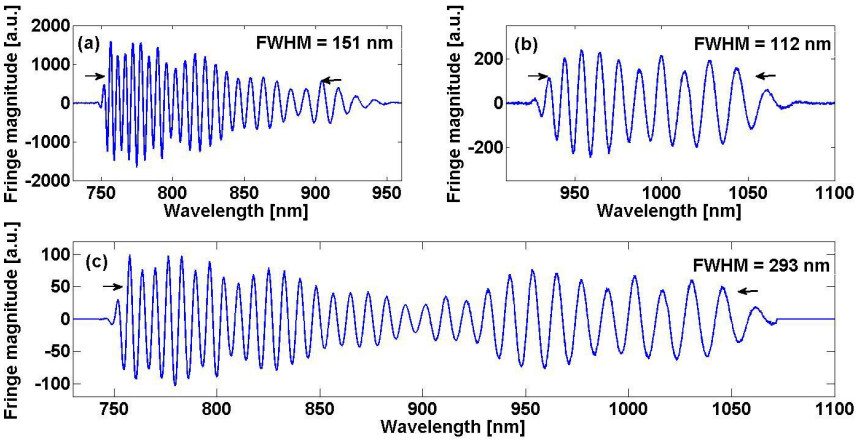

Figure 2: Spectral combination. Interference spectra acquired using a single reflective interface by (a) the Si camera and (b) the InGaAs camera. (c) Combined interference spectrum demonstrating an extended spectral range.

Due to the differences in the optical arrangements, the two spectra are linearized and resampled to the same wavelength space before combination. After finding the zero crossing points' coordinates of both spectrums at overlapping region (900nm ~ 1000nm) [a_1 a_2… a_n] for CCD1 and [b_1 b_2… b_m] for CCD2, a pair of a_i and b_j was chosen so that the periodicity of the two spectrums within overlapping region can match perfectly when superimposing one on the other. This means a_i of spectrum one corresponds to b_j of spectrum two. The (ai, bj) pair is unique in this case.]. The combined interference spectrum provides an extended FWHM spectral range of 293 nm centerd at 927.5 nm (Fig. 2c).

3.2 Axial and transverse resolution

We characterized the axial resolution of this system and obtained the axial point spread function (PSF) using a partial-reflecting mirror sample and the axial resolution was found to be ~1.27-μm in air, corresponding to 0.93 μm in tissue (n=1.36) (Fig. 3a). This matches well with the theoretical axial resolution of ~1.16μm in air. By changing the delay in the reference arm, the axial resolution decreases to ~ 1.7-μm at the depth around 500-μm when the signal reduced by 6-dB (fig. 3b).

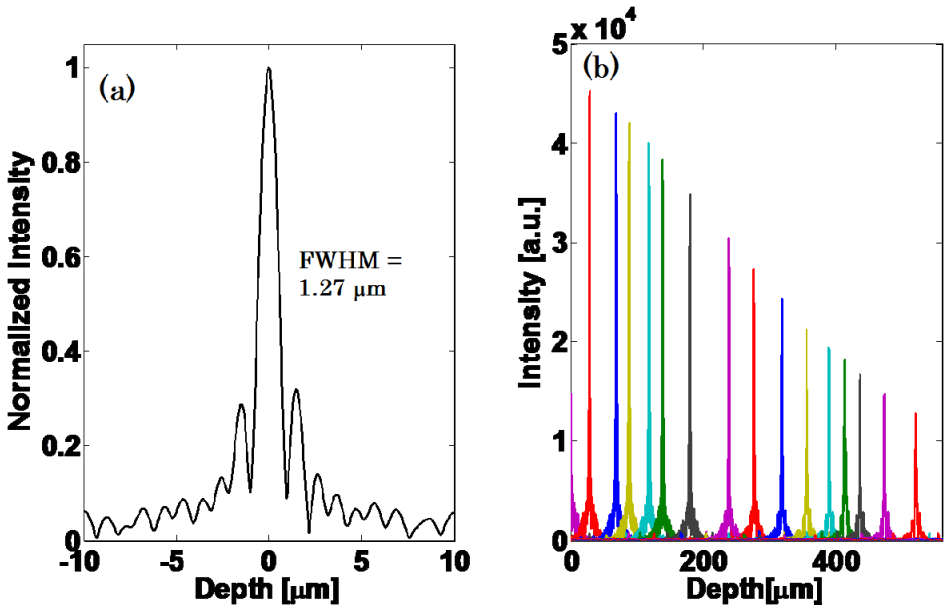

Figure 3 (a) Measured axial point-spread function using an attenuated mirror; (b) Measured axial PSFs on a linear scale for different delays relative to the reference arm length.

Fig. 4 demonstrates the transverse resolution using Edmund Optics resolution target in which group seven element six components can be clearly identified.

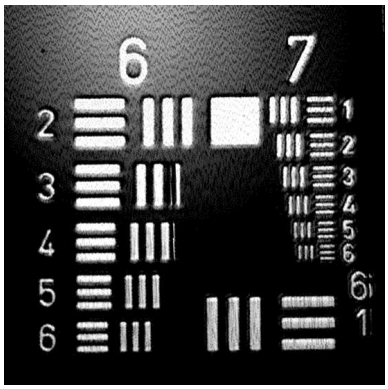

Figure 4: Image of Edmund Optics resolution chart demonstrating transverse resolution. Group seven elements six components can be clearly distinguished.

3.3 Sidelobe suppression

Because both cameras have weak responses at wavelength ~900-1000nm, the combined signal gave rise to pronounced sidelobe especially at the first order which limit the image quality of this system. Therefore, we developed a Gaussian Fit algorithm to reserve most part of the signal while strengthen the weak overlap part for sidelobe suppression. We first found the envelop of the interference signal and its corresponding Gaussian fitted amplitude (fig. 5). By comparing the signal envelope and the Gaussian fitted amplitude, the amplitude of the signal is strengthened/decreased to its Gaussian fitted amplitude if the difference between the signal envelop and its Gaussian fitted amplitude was above a predetermined threshold value. This method allows us to keep as much information as possible while enhance the weak signal to reduce the sidelobe. Several Gaussian Fit functions was used to determine the Gaussian fitted amplitude. After applying Fourier transform of the new signal with new envelope, the effect of sidelobe suppression can be demonstrated to be ~2-dB (fig. 3.9) without degradation in axial resolution.

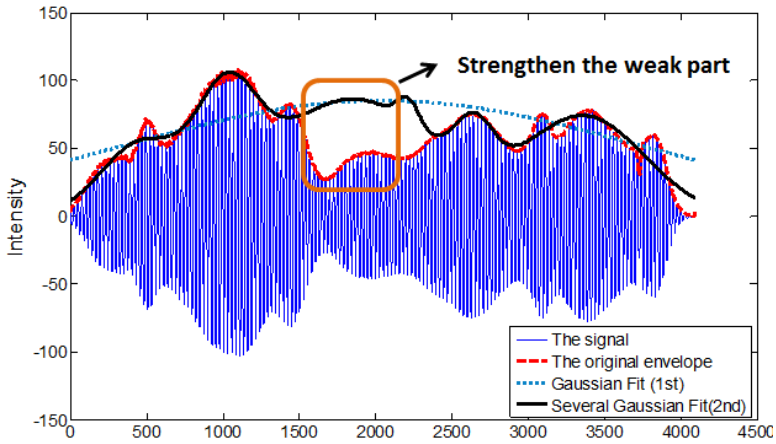

Figure 5: The process of Gaussian Fit. Red dashed curve, envelope of the original signal; blue dotted curve, 1st order signal Gaussian fit; black solid curve, new envelope

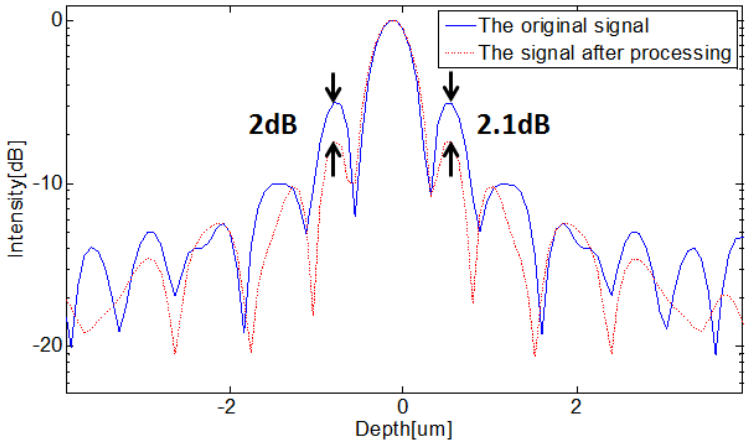

Figure 6: Point spread function of sidelobe suppressed signal in logarithm scale

3.4 Sensitivity

To characterize the sensitivity of the system, we measured the signal to noise ratio (SNR) using a partially-reflecting mirror sample (-40.7 dB reflectivity) when the path length difference between the mirror sample and reference arms was maintained at 0.1 mm. The sensitivity for the system (combined spectrum), Si camera alone, and InGaAs camera alone was measured to be 95.8 dB, 95.4 dB, and 91.1dB respectively. In order to understand the measured sensitivity values,

we analyzed the SNR in the case of individual camera based on previously established model [5-8]. The amount of noise generated per camera pixel was expressed in terms of the number of noise-equivalent electrons accumulated in each camera exposure (A-line) [8]. For the Si camera, the total electrical noise was estimated to be 846 e-. The relative intensity noise (RIN) was calculated to be 72 e- with the number of electrons per pixel generated by the reference arm light of 252,670 e-. At a scan rate of 10k Hz, the Si camera operated at an exposure time around 90 μs. The FWHM spectral bandwidth of the reference light received per pixel is 0.164 nm. For the mean spectrometer efficiency of 0.31 (including the grating diffraction efficiency, quantum efficiency of the sensor, and camera lens efficiency), a maximum SNR per pixel can be reach when the number of electrons per pixel generated by the reference arm light is equal to 257130 e- which corresponds to 215% of the full well depth (117500 e-). The number of shot noise electrons is 503 e-. Therefore, the total noise power of our system with the Si camera alone was 2.83 times larger than the shot-noise limit. The sum of electrons over the entire array generated by sample arm light returning from a 100% reflector was 2291100 e-. Therefore assuming a uniform spectral density, the sensitivity was predicted to be 98.44 dB. We think the difference between the measured sensitivity and the theoretical prediction is due to non-uniformity of the spectral response of both cameras.

In the case of InGaAs camera, the total electrical noise was estimated to be 872 e-. The RIN was calculated to be 56 e- with the number of electrons per pixel generated by the reference arm light of 158320 e-. Since the two cameras are synchronized, the line rate and the exposure time of the InGaAs camera was also 10k Hz and 90 μs respectively. The FWHM spectral bandwidth of the reference light received per pixel is 0.148 nm. For the mean spectrometer efficiency of 0.40, a maximum SNR per pixel can be reached when the number of electrons per pixel generated by the reference arm light is equal to 158320 e- which corresponds to 7.54% of the full well depth (2100000 e-). However, because the full well depth of the Si camera (312k e-) is 17.87 times smaller than that of the InGaAs camera, under the condition of a uniform input spectral density and a uniform spectral reflectivity of the reference arm, each InGaAs camera pixel was only 7.54% filled when the Si camera pixel was 219% filled. Therefore, the number of shot noise electrons is 398 e-, and the total noise power of our system with the InGaAas camera alone was 3.33 times larger than the shot-noise limit. The sum of electrons over the entire sensor generated by sample arm light returning from a 100% reflector was 1100200 e-. As a result, the sensitivity was predicted to be 93.46 dB. We attribute the difference between the measured sensitivity and the theoretical prediction to non-uniformity of the spectral response of the camera over the spectral range from 930 – 980 nm.

It is expected that the measured sensitivity after spectral combination is higher than the measured sensitivity of individual camera. This is because the two spetra has a ~100 nm overlap where the noise was suppressed relative to the signal based on the SNR model [5-8]. The InGaAs camera should have had ~5.5 dB higher sensitivity given enough reference light power in the range of 930-1105 nm. This problem can be solved by using a light source with higher power or more efficient system design. In addition, the sensitivity can be further improved by increasing the sample arm light power at the cameras using an objective lens with higher transmission rate and/or replacing BS3 with a dichroic filter.

4. *IN VIVO* EXPERIMENT

In vivo imaging was conducted using a well-established developmental biology animal model, the 3-day-old zebra fish larvae. Notochord can be clearly observed (fig 7.a). Furthermore, blood cells can be observed moving in tail artery under the notochord with identifiable upper and lower surfaces.

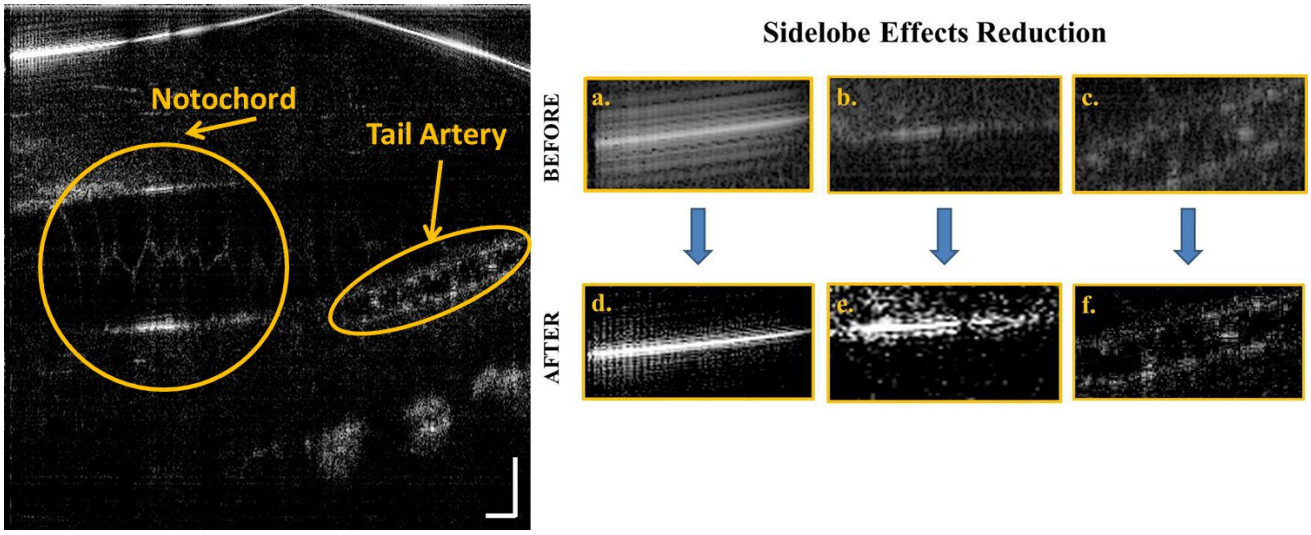

Figure 7: (a) Images of zebra fish notochord and moving blood cells. Scale bar: 50 μm; (b) Performance of sidelobe effect reduction.

5. CONCLUSION

In conclusion, we demonstrated a simultaneous dual light sources SD-OCT system which provides an ultrahigh axial resolution of 1.27μ-m in free space and 0.93-μm in tissue with comparable transverse resolution. Signal was detected by dual synchronized cameras and their spectrums were combined to achieve the ultrahigh axial resolution. An sidelobe suppression algorithm was developed to reduce the sidelobe by 2dB and improve the image quality. *In vivo* images were recorded using biology model of zebrafish larvae, in which the notochord, tail artery and individual red blood cells can be reliably visualized.

REFERENCES

[1]. O. Adegun, P. Tomlins, E. Hagi-Pavli, G. McKenzie, K. Piper, D. Bader, and F. Fortune, "Quantitative analysis of optical coherence tomography and histopathology images of normal and dysplastic oral mucosal tissues," Lasers Med Sci **27**, 795-804 (2012).

[2]. D. Huang, E. A. Swanson, C. P. Lin, J. S. Schuman, W. G. Stinson, W. Chang, M. R. Hee, T. Flotte, K. Gregory, C. A. Puliafito, and G. F. James, "Optical coherence tomography," Science **254**, 1178-1181 (1991).

[3]. G. J. Tearney, M. E. Brezinski, B. E. Bouma, S. A. Boppart, C. Pitris, J. F. Southern, and J. G. Fujimoto, "In Vivo Endoscopic Optical Biopsy with Optical Coherence Tomography," Science **276**, 2037-2039 (1997).

[4]. L. Liu, J. A. Gardecki, S. K. Nadkarni, J. D. Toussaint, Y. Yagi, B. E. Bouma, and G. J. Tearney, "Imaging the subcellular structure of human coronary atherosclerosis using micro-optical coherence tomography," Nat Med **17**, 1010-1014 (2011).

[5]. M. Choma, M. Sarunic, C. Yang, and J. Izatt, "Sensitivity advantage of swept source and Fourier domain optical coherence tomography," Opt. Express **11**, 2183-2189 (2003).

[6]. J. F. de Boer, B. Cense, B. H. Park, M. C. Pierce, G. J. Tearney, and B. E. Bouma, "Improved signal-to-noise ratio in spectral-domain compared with time-domain optical coherence tomography," Opt. Lett. **28**, 2067-2069 (2003).

[7]. R. Leitgeb, C. Hitzenberger, and A. Fercher, "Performance of fourier domain vs. time domain optical coherence tomography," Opt. Express **11**, 889-894 (2003).

[8]. S. Yun, G. Tearney, B. Bouma, B. Park, and J. de Boer, "High-speed spectral-domain optical coherence tomography at 1.3 μm wavelength," Opt. Express **11**, 3598-3604 (2003).